



# A Candidate Period of 4.605 Days for FRB 20121102A and One Possible Implication of Its Origin

Jixuan Li<sup>1</sup>, Yang Gao<sup>1</sup> , Di Li<sup>2,3</sup> , and Kinwah Wu<sup>4</sup>

<sup>1</sup> School of Physics and Astronomy, Sun Yat-Sen University, Zhuhai, 519082, Guangdong, People's Republic of China

<sup>2</sup> CAS Key Laboratory of FAST, National Astronomical Observatories, Chinese Academy of Sciences, Beijing 100101, People's Republic of China

<sup>3</sup> Research Center for Intelligent Computing Platforms, Zhejiang Laboratory, Hangzhou 311100, People's Republic of China

<sup>4</sup> Mullard Space Science Laboratory, University College London, Holmbury St. Mary, Surrey, RH5 6NT, UK

Received 2022 August 30; revised 2024 April 17; accepted 2024 April 17; published 2024 June 25

## Abstract

A firm establishment of the presence or the lack of periodicity in repeating fast radio bursts is crucial for determining their origins. Here, we compile 1145 radio bursts of FRB 20121102A with fluence larger than 0.15 Jy ms from observations using the Five-hundred-meter Aperture Spherical radio Telescope, the Arecibo Observatory, the Green Bank Telescope, the Effelsberg Telescope, the MeerKAT Telescope, the Lovell Telescope, the Deep Space Network 70 m radio telescopes, the Very Large Array, and the Westerbork Synthesis Radio Telescope, spanning the time interval of MJD 57175–58776. A quasi-period of  $157.1^{+5.2}_{-4.8}$  days and a candidate quasi-period of  $4.605^{+0.003}_{-0.010}$  days are found through the phase-folding probability binomial analysis. The former is consistent with previous findings and the latter is new. The 4.605 day periodicity is more obvious in high-energy bursts with fluence larger than  $1 \times 10^{38}$  erg. The presence of these (candidate) quasi-periods, together with the corresponding width of burst accumulation in the phase space, are consistent with the bursts originating from a binary degenerate star system with a close-by planet around the primary neutron star.

*Unified Astronomy Thesaurus concepts:* [Radio transient sources \(2008\)](#); [Radio bursts \(1339\)](#); [Star-planet interactions \(2177\)](#); [Time series analysis \(1916\)](#)

*Supporting material:* machine-readable table

## 1. Introduction

High-cadence observations led to the discovery of fast radio bursts (FRBs), which usually have millisecond durations and are detected at frequencies between 110 MHz and 8 GHz (Lorimer et al. 2007; Gajjar et al. 2018; Pleunis et al. 2021; Niu et al. 2022). More than 700 FRB sources have been identified, with 50 repeaters among them (CHIME/FRB Collaboration et al. 2023). The host galaxies of some FRBs have been localized, the polarization and energy of bursts have been measured, and the energy distribution and period of activities have been identified for a few repeating sources (Zhang 2020b; Petroff et al. 2022). FRBs are now believed to originate from a neutron star or magnetar through reconnection-driven free-electron laser emission (Lyutikov et al. 2020; Lyutikov 2021), coherent curvature radiations (Kumar et al. 2017; Lu et al. 2020; Wang et al. 2022), or synchrotron maser emissions (Metzger et al. 2019). The finding of periodic activities from repeating sources suggests that the repeaters likely have progenitors in binary systems (The CHIME/FRB Collaboration 2020; Zhang 2020c) or originate from the precessions of flaring magnetars (Levin et al. 2020).

For the repeating source FRB 20121102A, a period of  $\sim 160$  days was found from extensive observations (Cruces et al. 2018; Rajwade et al. 2020). The Five-hundred-meter Aperture Spherical radio Telescope (FAST) observations of this source revealed a bimodal burst energy distribution, hinting at different mechanisms or emission sites of the

source (Li et al. 2021). The time-domain behaviors may be linked to the energy distribution. We thus carried out a comprehensive periodicity analysis of FRB 20121102A, based on data from the leading radio telescopes (Spitler et al. 2016, 2018; Chatterjee et al. 2017; Hardy et al. 2017; Law et al. 2017; Marcote et al. 2017; Scholz et al. 2017; Cruces et al. 2018; Gajjar et al. 2018; Michilli et al. 2018; Gourdji et al. 2019; Hessels et al. 2019; Caleb et al. 2020; Majid et al. 2020; Oostrum et al. 2020; Pearlman et al. 2020; Rajwade et al. 2020; Hilmarsson et al. 2021; Li et al. 2021; Hewitt et al. 2022; Jahns et al. 2023).

The period of about 160 days detected in FRB 20121102A is a quasi-period with a  $>50\%$  duty cycle (Cruces et al. 2018; Rajwade et al. 2020). This behavior is similar to the radio bursts from star–planet and Jupiter–satellite systems (Zarka et al. 2018). Searching for such quasi-periods requires methods beyond the Fourier transformation in which the period is the only parameter. An improved methodology needs to consider the variable width of the bursts' distribution in the phase diagram. The minimum-string-length method developed in analyzing the periods of variable stars allows such variations (Dworetzky 1983). When studying the periodicity of bursts from exoplanet systems, Gao (2021) introduced the width of the burst duty cycle as another parameter in addition to the period. They explored different candidate periods by folding the time series of bursts to the phase space, and then testing different locations and widths of the duty cycles within which the bursts occur. By adopting this method, some of the bursts from the star–planet system HD 189733 are found to be correlated with the planet. The method is potentially applicable to repeating FRBs, in which the burst duty cycle may also vary and affect the detection of periods in conventional



Original content from this work may be used under the terms of the [Creative Commons Attribution 4.0 licence](#). Any further distribution of this work must maintain attribution to the author(s) and the title of the work, journal citation and DOI.

**Table 1**  
Examples of FRB 20121102A Bursts in Data Set II

ID	MJD	Ref.	Telescope	Frequency (MHz)	Fluence $\geq$ (Jy ms)	Observation Length (hr)	Corrected Count Rate (ct hr <sup>-1</sup> )
1	57175.69314	a	Arecibo	1214–1537	0.15	1.75	0.57
2	57175.74351	a	Arecibo	1214–1537	0.15	1.75	0.57
3	57175.74566	a	Arecibo	1214–1537	0.15	1.75	0.57
4	57175.74762	a	Arecibo	1214–1537	0.15	1.75	0.57
5	57175.74828	a	Arecibo	1214–1537	0.15	1.75	0.57
6	57339.35604	b	GBT	1600–2400	0.15	0.83	1.20
...	...	...	...	...	...	...	...
1143	58766.94890	c	FAST	1050–1450	0.15	1.00	1.00
1144	58772.93022	c	FAST	1050–1450	0.15	1.00	1.00
1145	58776.85096	c	FAST	1050–1450	0.15	1.00	1.00

**Notes.** References: (a) Spitler et al. (2016); (b) Scholz et al. (2016); and (c) Li et al. (2021). A full version of this list is available in machine-readable format. A .tar.gz archive containing data sets I and II can be downloaded from the online version of this article.

(This table is available in its entirety in machine-readable form.)

periodograms. In this paper, we further improve this method and apply it to FRB 20121102A.

The data are discussed in Section 2; in Section 3, we present the quasi-period searching method and the results for FRB 20121102A; the implications of the burst origins are given in Section 4; and conclusions are made in Section 5.

## 2. Data Collection

There are two data sets of FRB 20121102A bursts used in this paper for the period analysis. The first data set (data set I) summarizes the bursts detected by FAST (Li et al. 2021; Zhang et al. 2024), the Arecibo Observatory (AO; Spitler et al. 2016, 2018; Chatterjee et al. 2017; Hardy et al. 2017; Marcote et al. 2017; Scholz et al. 2017; Michilli et al. 2018; Gourdji et al. 2019; Hessels et al. 2019; Hilmarsson et al. 2021; Hewitt et al. 2022; Jahns et al. 2023), the Effelsberg Telescope (Hardy et al. 2017; Cruces et al. 2018; Spitler et al. 2018; Hilmarsson et al. 2021), the Very Large Array (Law et al. 2017; Hilmarsson et al. 2021), the Green Bank Telescope (GBT; Scholz et al. 2017; Gajjar et al. 2018; Michilli et al. 2018; Hessels et al. 2019), the Lovell Telescope (Rajwade et al. 2020), the Westerbork Synthesis Radio Telescope (Oostrum et al. 2020), the MeerKAT telescope (Caleb et al. 2020), and the Deep Space Network telescopes (Majid et al. 2020; Pearlman et al. 2020). In order to calculate the energy-corrected burst rate in the period analysis (see Section 3.1 for details), bursts with fluences larger than or equal to 0.15 Jy ms are kept in the list. This means we have excluded bursts with energy smaller than this threshold, including the weak detections from FAST (Li et al. 2021), AO (Spitler et al. 2016; Hilmarsson et al. 2021; Hewitt et al. 2022; Jahns et al. 2023), the Effelsberg Telescope (Cruces et al. 2018; Hilmarsson et al. 2021), and GBT (Zhang et al. 2013). Additionally, the 12 Jy ms burst detected by the Canadian Hydrogen Intensity Mapping Experiment telescope (Joseph et al. 2019) is not included, because of its large fluence and short observation length, which lead to an excessive count rate. The first data set finally includes 1145 bursts and can be downloaded in machine-readable format from the online journal, with an example shown in Table 1. For each burst, the detection threshold of the burst fluence, the length of the observation session, and the count rate corrected by the fluence threshold are given.

The second data set (data set II) contains high-energy bursts with fluences  $> 5 \times 10^{38}$  in FAST observations or equivalently  $> 0.4$  Jy ms in AO observations. As a high-energy subset of data set I, data set II contains 289 bursts (see Table 1 .tar.gz archive). More details of the data set can be found in Li et al. (2021), Hewitt et al. (2022), and Jahns et al. (2023).

## 3. Quasiperiodicity Analysis

### 3.1. Method

Bursty phenomena like solar and stellar flares have higher occurrence rates in their “active regions” or when the binaries/planets are in specific ranges of orbital positions (Dulk 1985; Pérez-Torres et al. 2021). In such circumstances, the bursts as a time series accumulate in relative phases of the solar/stellar rotation or binary/planet orbit. A study of this kind of quasiperiodicity should target two parameters, i.e., the period and the width of the active sector in the phase space. The method of finding these two parameters is essentially phase folding, i.e., for one burst, its phase  $P'$  when assuming a test period  $T$  is calculated from the event MJD as

$$\text{MJD} - 56,000 = CT + P'T, \quad (1)$$

where 56,000 is subtracted from the MJD for the convenience of computing,  $C$  is an integer, and  $0 \leq P' < 1$ . We then introduce the test central active phase  $P$  and its half-width  $\Delta P$  ( $0 < \Delta P \leq 0.5$ ) and count the number of bursts with their phases:

$$\begin{aligned} P' &\in [P - \Delta P, P + \Delta P] && (P - \Delta P \geq 0 \text{ \& } P + \Delta P \leq 1), \\ P' &\in [0, P + \Delta P) \cup [P - \Delta P + 1, 1) && (P - \Delta P < 0), \\ P' &\in [0, P + \Delta P - 1) \cup [P - \Delta P, 1) && (P + \Delta P > 1). \end{aligned} \quad (2)$$

This number of bursts is noted as  $N(T, P, \Delta P)$ , which can be normalized by the total number of bursts, namely

$$\hat{N}(T, P, \Delta P) = \frac{N(T, P, \Delta P)}{N(T, P, 0.5)}. \quad (3)$$

For a phase-independent distribution of bursts,  $\hat{N}$  does not change when the test central active phase  $P$  varies. Contrarily, if  $\hat{N}$  has variations above the random fluctuation and becomes significantly large for a test phase  $P$  in a certain test period  $T$ , the bursts likely have an intrinsic period  $T$  and tend to occur

around the test phase  $P$  within half the sector width  $\Delta P$ . Such burst accumulation can be quantitatively checked by assuming a phase-independent burst distribution and calculating the possibility that  $\hat{N}(T, P, \Delta P)$  is equal to or larger than its current value. This is simply the cumulative probability that  $N(T, P, \Delta P)$  or more of the total  $N(T, P, 0.5)$  bursts occur in the  $2\Delta P$  phase range, i.e.,

$$F[N(T, P, \Delta P); N(T, P, 0.5), 2\Delta P] = \sum_{x=N(T, P, \Delta P)}^{N(T, P, 0.5)} B[x; N(T, P, 0.5), 2\Delta P], \quad (4)$$

where

$$B(x; N, 2\Delta P) = C_N^x (2\Delta P)^x (1 - 2\Delta P)^{N-x} \quad (5)$$

is the probability of the occurrence of  $x$  events in  $N$  experiments, each following a binomial distribution with single event probability  $2\Delta P$  (the whole phase range is unity).

In actual period searches, the cumulative probability  $F$  defined in Equation (4) can be calculated when one particular parameter set is tested. As the number of independent periods (frequencies), central active phases, and phase widths searched increases, the minimum value of  $F$  becomes smaller compared to one particular test. We take into account this effect by following the definition of false-alarm probability (FAP) in Horne & Baliunas (1986) and VanderPlas (2018), i.e.,

$$\text{FAP} = 1 - (1 - F)^{N_p N_{\Delta P} N_{\text{eff}}}. \quad (6)$$

Here,  $F$  is calculated using Equation (4) for a particular test and FAP is the probability that the detected burst accumulation in the test would be achieved under the phase-independent burst assumption.  $N_p$  and  $N_{\Delta P}$  are the numbers of  $P$  and  $\Delta P$  searched in the trials, close to the independent values of these two parameters.  $N_{\text{eff}}$  is the number of independent frequencies that can be calculated from

$$N_{\text{eff}} = f_{\text{Ny}} \Delta T, \quad (7)$$

with  $f_{\text{Ny}}$  being the Nyquist frequency and  $\Delta T$  the maximum time interval in the period search. For both data set I and data set II,  $\Delta T$  is approximately 1600 days. For irregularly spaced time series, the Nyquist frequency can be estimated as (Koen 2006)

$$f_{\text{Ny}} = \frac{0.5}{\delta_*}, \quad (8)$$

with  $\delta_*$  being the precision of the time measurements, which is 10 ms in this paper. After calculating FAP, the confidence ( $\sigma$ ) level  $Z$  can be estimated through the distribution function of the standard Gaussian distribution (Carpano et al. 2007; Forbes et al. 2011), i.e.,

$$1 - \text{FAP} \approx \frac{1}{\sqrt{2\pi}} \int_{-Z}^Z e^{-\frac{x^2}{2}} dx. \quad (9)$$

If FAP is in close proximity to zero, the phase-independent assumption of bursts can be ruled out and the intrinsic accumulation of bursts with period  $T$ , central active phase  $P$ , and half-sector-width  $\Delta P$  can be confirmed at the confidence level  $Z$ . The above method is named phase-folding probability binomial analysis (PBA).

Before adopting the above periodicity analysis, we make two additional corrections on the observation length and detection

threshold when counting the bursts of FRB 20121102A. First, the uneven and sometimes periodic distribution of the observation window and its width may lead to pseudo-periods of the bursts. However, the effect of the width of the window can be partially avoided by using the count rate instead of the number of bursts during a continuous observation session. The count rate (around the central active phase  $P$  with half-sector-width  $\Delta P$ ) for bursts observed during a continuous session  $i$  with length of observation time  $\tau_i$  is

$$n_i(T, P, \Delta P) = \frac{N_i(T, P, \Delta P)}{\tau_i}, \quad (10)$$

where  $N_i(T, P, \Delta P)$  is the number of bursts detected in this observation session. The total count rate in an observation campaign is the sum of the above rate over all observation sessions, i.e.,

$$n(T, P, \Delta P) = \sum_i n_i(T, P, \Delta P). \quad (11)$$

The normalized count rate is accordingly

$$\hat{n}(T, P, \Delta P) = \frac{n(T, P, \Delta P)}{n(T, P, 0.5)}. \quad (12)$$

Second, when considering bursts detected by different telescopes, they usually have different lower limits of fluences. In the same observation session toward a repeating source, the bursts recorded by a telescope with a higher fluence threshold will be less than those recorded by a telescope with a lower fluence threshold. This bias can be corrected for FRB 20121102A, as we know the energy distribution of its bursts. All bursts in data set I have fluences equal to or higher than 0.15 Jy ms, above which the generalized Cauchy function of the energy distribution in Li et al. (2021) can be simplified to a constant + a power law. For bursts with fluences between 0.15 and 0.24 Jy ms, corresponding to  $\sim 2$  and  $3 \times 10^{38}$  erg in FAST observations, the burst rate can be treated as a constant (Figure 2 in Li et al. 2021). For bursts with fluences larger than 0.24 Jy ms, the energy distribution follows a power law (Table 1 of Li et al. 2021). So, if we assume this distribution also applies for bursts detected by other telescopes, the energy distribution function for data set I is<sup>5,6</sup>

$$\begin{aligned} p(E) &= p(0.24) & (0.15 \leq E < 0.24), \\ p(E) &= p(0.24) \left( \frac{E}{0.24} \right)^{-1.37} & (E \geq 0.24), \end{aligned} \quad (13)$$

where  $E$  is the burst energy in Jy ms. To correct the count rates of bursts detected by telescopes at different fluence thresholds, we further integrate the above distribution function from the threshold energy  $E$  to  $+\infty$  and get

$$\begin{aligned} f(E) &= \int_E^{+\infty} p(E') dE' = \frac{0.89 - E}{0.74} & (0.15 \leq E < 0.24), \\ f(E) &= \int_E^{+\infty} p(E') dE' = \frac{0.24^{1.37}}{0.74 \cdot 0.37 \cdot E^{0.37}} & (E \geq 0.24), \end{aligned} \quad (14)$$

<sup>5</sup> The distribution function is achieved by assuming the detection rates are normalized by the rate at a fluence of 0.15 Jy ms. It is also noted that the FAST survey is complete for fluences larger than 0.15 Jy ms (Li et al. 2021).

<sup>6</sup> The variation of the energy distribution with burst frequency is not considered here, which may lead to an overestimate or underestimate of the normalized equivalent count rate for the bursts detected in frequencies other than 1.05–1.45 GHz.

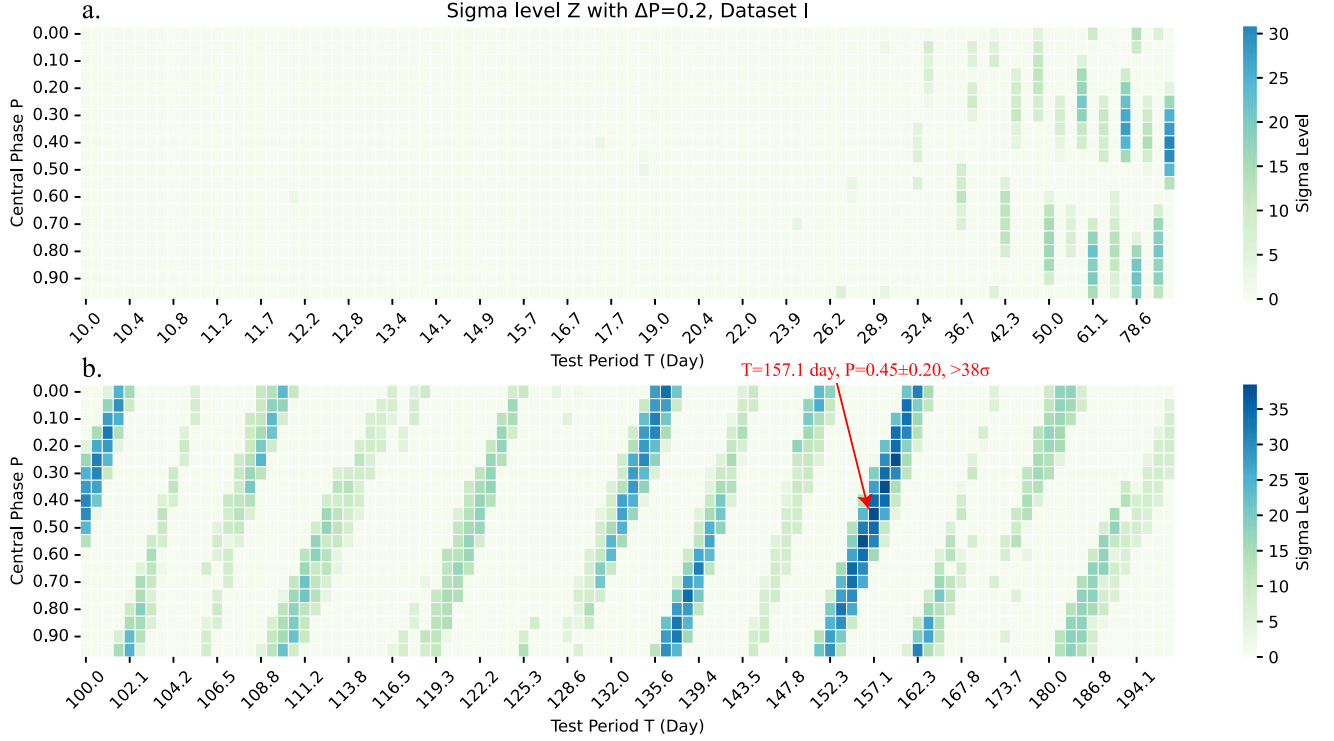


**Figure 1.** The distribution of  $\sigma$  level  $Z$  for test periods from 10 to 100 days (a) and from 100 to 200 days (b), with the test central active phase from 0 to 0.95 and half-width  $\Delta P = 0.2$ , calculated for data set I. The colors of the pixels show the  $\sigma$  level  $Z$ . A high  $\sigma$  level is found at  $T = 157.1$  days at central active phase  $P = 0.45$  with  $Z > 38$ . The presence of the high- $\sigma$ -level pixels indicates the existence of a period of around 157.1 days.

which is the detection rate (normalized by  $f(0.15)$ ) for bursts with energy higher than  $E$ . We adopt it and calculate from the count rate of an observation  $j$  with threshold energy  $E_j$  to get the equivalent count rate with threshold 0.15 Jy ms, i.e.,

$$n_{0.15, E_j}(T, P, \Delta P) = \frac{n_{E_j}(T, P, \Delta P)}{f(E_j)}. \quad (15)$$

Summing the above rate over all observations with their corresponding fluence thresholds,

$$n_{0.15}(T, P, \Delta P) = \sum_j n_{0.15, E_j}(T, P, \Delta P) \quad (16)$$

is the total count rate for a data set, equivalently at 0.15 Jy ms. Its normalized form is

$$\hat{n}_{0.15}(T, P, \Delta P) = \frac{n_{0.15}(T, P, \Delta P)}{n_{0.15}(T, P, 0.5)}. \quad (17)$$

As a summary, practically each burst is counted as one divided by its observation length  $\tau_i$  and the energy correction function  $f(E_j)$  in the PBA procedure. For data set I, we do the period analysis based on  $\hat{n}_{0.15}(T, P, \Delta P)$ , the normalized equivalent count rate with a threshold of 0.15 Jy ms. For data set II, since all detections have the same energy threshold, the period analysis is carried out by simply accounting for the observation window function to the probability for a single burst to occur within a phase range. That is, by replacing  $2\Delta P$  in Equation (4) with the normalized observation window function  $W(T, P, \Delta P)$ , i.e., the normalized observation time spent within the region with central active phase  $P$  and

half-width  $\Delta P$ , the PBA is made upon the number of bursts  $N_i(T, P, \Delta P)$ .

### 3.2. Results

#### 3.2.1. Period of 157.1 Days

The FAP is first calculated based on data set I. Test frequencies from  $10^{-1}$  to  $100^{-1} \text{ days}^{-1}$  and  $100^{-1}$  to  $200^{-1} \text{ days}^{-1}$  with equal frequency steps of  $1000^{-1} \text{ days}^{-1}$  and  $20,000^{-1} \text{ days}^{-1}$  are explored, respectively. For each test frequency, test central active phases from  $P = 0.00$  to  $0.95$  with a  $0.05$  step are adopted, covering the entire phase space if the width of the active sector is not smaller than  $0.05$ . The distribution of the confidence level  $Z$  for the half-active-phase  $\Delta P = 0.2$  is shown in Figure 1. It is noted that high- $\sigma$  confidence levels occur around period  $T = 157.1$  days and central active phase  $P = 0.45$ . For the test period  $T = 157.1$  days, the high- $\sigma$ -level squares spread to segments covering 20% of the entire phases, demonstrating the accumulation of bursts being in a wide phase range. The effect of the observation window function is excluded from this period (Figure 2; see also Cruces et al. 2018). An uncertainty of  $^{+5.2}_{-4.8}$  days can be estimated, outside of which the sum of the normalized count rate within the active phase decreases to be  $\hat{n}_{0.15}(T, P, 0.2) < 0.90$ , significantly smaller than the value for 157.1 days in the  $\Delta P = 0.2$  trial. The phase distributions of the normalized count (rate) and window function for the 157.1 day period are shown in Figure 2. The window function is the observation length at each continuous observation, with data extracted from Scholz et al. (2016, 2017), Spitler et al. (2016, 2018), Hardy et al. (2017), Law et al. (2017), Cruces et al. (2018), Gajjar et al. (2018), Michilli et al. (2018), Caleb



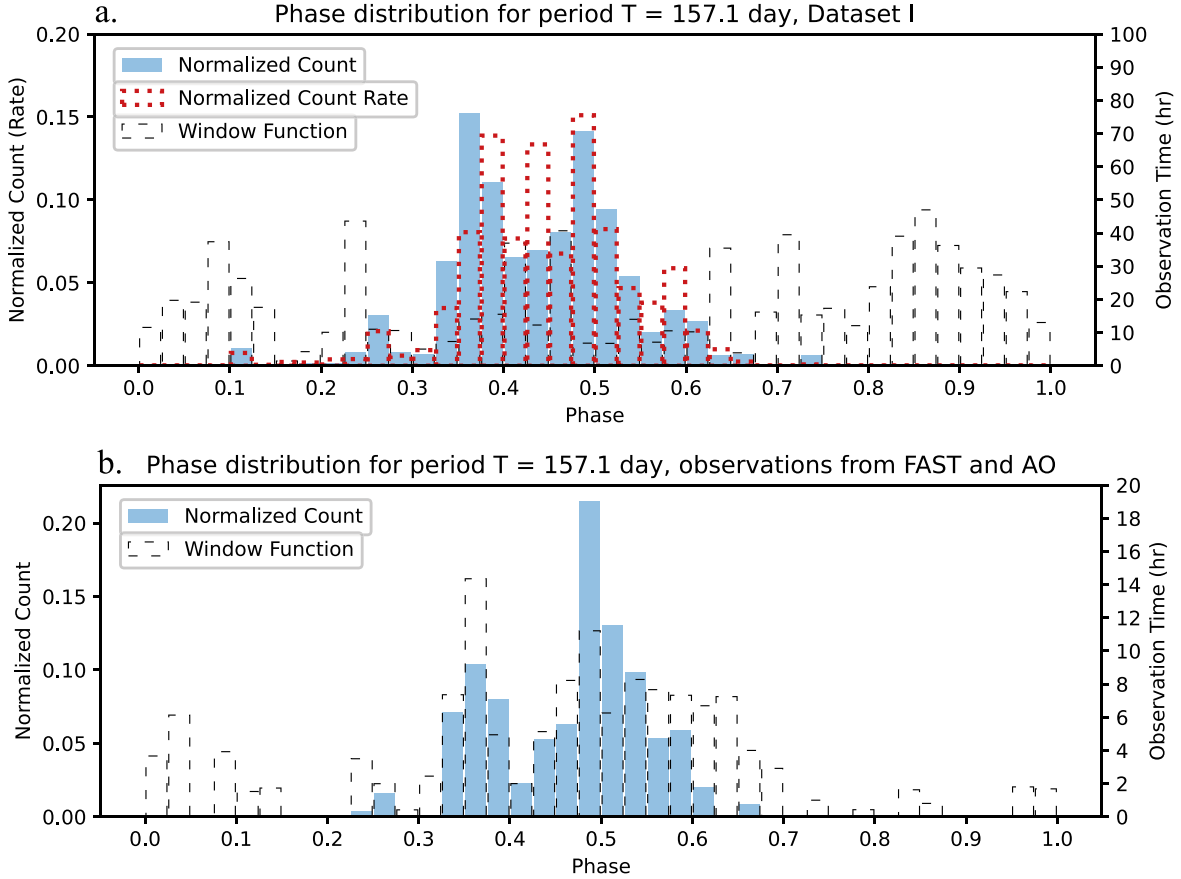


**Figure 2.** For a period of 157.1 days, the phase distribution is plotted for data set I (a) and for observations from FAST and AO (b). The blue, dotted red, and dashed black histograms are the normalized burst counts  $\hat{N}$  (see Equation (3)), the normalized count rate  $\hat{n}_{0.15}$  (see Equation (17)), and the observation window, respectively. Almost all the bursts concentrate at phases 0.325–0.625, and most of the observations from FAST and AO are made within this duty cycle (b).

et al. (2020), Majid et al. (2020), Pearlman et al. (2020), Rajwade et al. (2020), Li et al. (2021), Hewitt et al. (2022), and Jahns et al. (2023). It is seen that the count peaks at phases between 0.35 and 0.6, with the bursts spreading to  $\sim 50\%$  of the phases in data set I. Most of the observation windows of FAST and AO are within the duty cycle (see panel (b)).

However, high- $\sigma$ -level squares are found in other periods/phases as well, according to Figure 1. Do they also indicate intrinsic periods or are they caused by the 157.1 day period? From Equation (1), when we slightly change the test period from  $T$  to  $T + \delta T$ , the change of the phase for a burst is

$$\delta P' \approx -\frac{C}{T} \delta T. \quad (18)$$

According to Table 1, for the 157.1 day period, cycle  $C$  is between 7 and 17 for the bursts in data set I. The bursts in each cycle have a specific “curve” in Figure 1, and they meet at the high- $\sigma$  squares around  $T = 157.1$  days, indicating the existence of an intrinsic period for bursts in different cycles. They gradually disperse in the phase space when the test period goes away from the intrinsic period of 157.1 days. So the phase concentrations for  $T > \sim 80$  days in Figure 1 (mainly in panel (b)) are likely due to the intrinsic period of 157.1 days. Also, trial periods  $> \sim 10$  days (panel (a)) have been studied at a high confidence level in Rajwade et al. (2020) and Cruces et al. (2018), where no other intrinsic period is found. We then seek for possible periods between 2 and 10 days in this paper.

### 3.2.2. Period of 4.605 Days

The PBA method is carried out for test frequencies from  $2^{-1}$  to  $10^{-1}$  days $^{-1}$  with an equal frequency step of  $250^{-1}$  days $^{-1}$  (corresponding to a test period from  $T = 2$  to 10 days with approximately a  $\sim 0.01$  day step). For each test period, test central active phases from  $P = 0$  to 0.95 with a 0.05 step are adopted, and a half-active-phase  $\Delta P = 0.025$ –0.2 with step size 0.025 is considered. The results with half-width  $\Delta P = 0.05$  for data sets I and II are shown in Figure 3. For data set I, there are clearly 2, 3, 4, 5, and 6 day periods arising from the approximately 1 day period of the observation window (Figure 3(a)). A local high- $\sigma$  square with a test period of 4.605 days is identified in data set II (Figure 3(b)). At this test period, a high-confidence-level pixel is also found for data set I (Figure 3(a)) with the same central active phase, suggesting the existence of an intrinsic period of 4.605 days. For the total 1145 bursts in data set I, 252 bursts occur in the  $0.70 \pm 0.05$  phase range, for which  $\text{FAP} = 7.97 \times 10^{-20}$ , corresponding to a  $9.04\sigma$  confidence level. For data set II, 98 of the total 289 bursts are detected within the  $0.70 \pm 0.05$  phase range, with the  $\text{FAP} = 1.35 \times 10^{-18}$ , corresponding to  $8.72\sigma$ . The uncertainty of the period is estimated to be  $^{+0.003}_{-0.010}$  days, outside of which the confidence level decreases to less than  $4\sigma$  for both data sets I and II.

The phase distribution for the period of 4.605 days is shown in Figure 4. For both data sets, the phase distributions show peaks at the active phase  $0.70 \pm 0.05$ , with the concentration of



**Figure 3.** The distribution of  $\sigma$  level  $Z$  for test periods from 2 to 10 days and the test central active phase from 0 to 0.95, calculated for data set I (a) and data set II (b). The colors of the pixels show the  $\sigma$  level  $Z$ . The black-edged boxes in (a) show the results where  $T$  is close to integers of 2, 3, 4, 5, and 6 days. For  $T = 4.605$  days, high  $\sigma$  level  $Z = 9.04$  and  $8.72$  are found at  $P = 0.70$  for data set I and data set II respectively.

bursts being more obvious for data set II, containing high-energy bursts (Figure 4(b)). To find the lower-energy cutoff of the 4.605 day period, we divide the bursts observed by FAST and AO into six groups according to their fluences. The confidence level of the 4.605 day period is calculated for each group of bursts, shown in Figure 5 with corresponding phase distributions. High confidence levels are reached when the burst fluence is higher than  $5 \times 10^{38}$  erg (Figure 5 (a)) or between  $1 \times 10^{38}$  erg and  $3 \times 10^{38}$  erg (Figures 5 (c) and (d)). There is a drop of the confidence level for bursts with fluences between  $3 \times 10^{38}$  erg and  $5 \times 10^{38}$  erg, but the concentration of bursts can still be seen at the same phase interval (Figure 5(b)). For bursts with fluences lower than  $1 \times 10^{38}$  erg, the confidence level decreases to  $\sim 0$  and the concentration of bursts is no longer seen (Figures 5(e) and (f)). Therefore, the  $4.605^{+0.003}_{-0.010}$  day period is an intrinsic property for bursts with fluences higher than  $1 \times 10^{38}$  erg. This low-energy cutoff of periodicity is roughly consistent with the  $3 \times 10^{38}$  erg threshold of the bimodal energy distribution in Li et al. (2021).

Furthermore, this period is a quasi-period in the sense that only some of the bursts concentrate in the active phase. This is similar to the radio bursts from the interactions of Jupiter with its satellites Io and Ganymede, which have periods related to the orbits of the satellites. The orbital periods only apply to  $\sim 30\%$  (bursts related to Io) and  $\sim 6\%$  (bursts related to Ganymede) of all observed bursts from the Jovian system, with the rest from Jupiter alone (Zarka et al. 2018). To summarize, the accumulation of bursts shown in Figure 4 is a rare event if the bursts distribute evenly with phase. So we conclude at a confidence level higher than  $8\sigma$  the existence of the candidate

period 4.605 days and the accumulation of some of the bursts in the specific active phase range of  $0.70 \pm 0.05$ . The reason it is called a “candidate” period is that the sampling effect of discrete observations should be checked by future observations.

We have also explored the periodicity of bursts near  $T = 4.6$  days using other methods. The  $\chi$ -square test (Leahy et al. 1983) and H test (De Jager et al. 1989; De Jager & Büsching 2010) give  $\chi$ -squares and  $H$ s larger than the average near 4.6 days, but all of these values are much lower compared to those in the vicinity of integer numbers of days. These results are consistent with the PBA result of 4.605 days, but cannot be considered as candidate periods from the methods themselves, due to the existence of many other local peaks. The Lomb–Scargle (LS) periodogram (VanderPlas 2018) for data set I detects a period at 160 days (Figure 6 (a)), which is consistent with the results of Rajwade et al. (2020) and Cruces et al. (2018). However, no period can be found between 1 and 10 days using LS, except the 1 day period from the observation windows (Figures 6(b) and (c)). The quadratic mutual information (QMI) analysis (Huijse et al. 2018), generated by the Python package frbpa,<sup>7</sup> shows 1 day and 2 day periods of the observation window, with no period near 4.6 days found (Figures 7 (a) and (b)). Wavelet analysis has also been tested for data sets I and II, but no period was found. The period of 4.605 days has a small duty cycle of 0.10, as seen from Figure 4, making it hard to be detected in the wavelet analysis, the LS periodogram, and the QMI analysis, which are based on the Fourier transform. Probability analysis methods such as the

<sup>7</sup> Available at [github.com/KshitijAggarwal/frbpa](https://github.com/KshitijAggarwal/frbpa).

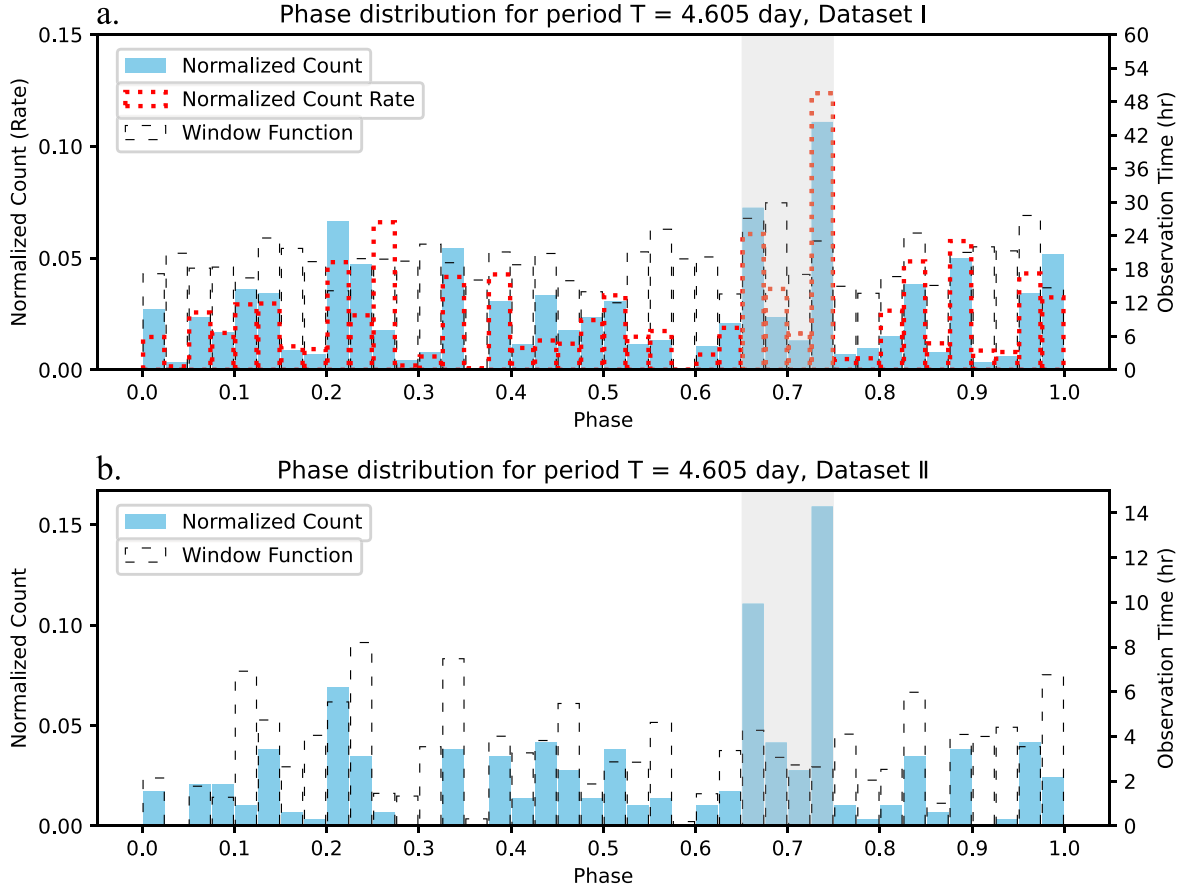


**Figure 4.** For the period of 4.605 days, the phase distribution is plotted for data sets I (a) and II (b). The blue, dotted red, and dashed black histograms are the normalized burst counts  $\hat{N}$  (see Equation (5)), the normalized count rate  $\hat{n}_{0.15}$  (see Equation (17)), and the observation window, respectively. The active phase is shown by the gray region. Some of the bursts concentrate at phase  $0.70 \pm 0.05$  for both data sets.

$\chi$ -square test, H test, and PBA could be more applicable to periods of bursty phenomena with small duty cycles. In particular, the PBA method is more sensitive to such quasi-periods, as it is in principle a  $\chi$ -square test, but more specifically based on the single-active-phase assumption.

To quantify the different sensitivities of PBA and the LS periodogram, we generate 1000 sets of burst data through Monte Carlo simulation and apply the two methods to the data sets. Taking data set II as a reference, each set of simulation data contains 28% bursts with 0.1 duty cycle, 4.605 day periodicity, and 72% random bursts with no periodicity. The same observation window of data set II is then applied to the simulation data, resulting in “detected” bursts ranging from 250 to 310 for each data set. The confidence levels of the 4.605 day period are calculated using PBA and LS respectively, with the distributions shown in Figure 8(a). The LS periodogram always gets a  $<1\sigma$  confidence level, while PBA detects the 4.605 day period at confidence levels between  $4\sigma$  and  $10\sigma$ . We also show in Figure 8(b) the number of false detections of periodicity in PBA. A false detection is the detection of a period other than close to 4.605 days, at which the confidence level is higher than that of 4.605 days. In  $> \sim 85\%$  sets of simulation data, there are less than three false detections, so the detection of the 4.605 day period by PBA is seldom confused by false detections. The above results show that PBA is more sensitive than LS when some (28% here) of the bursts have a small duty cycle (0.1 here) periodicity.

## 4. Discussions on the Burst Origin and Formation of FRB 20121102A

### 4.1. Possible Origin of the Radio Emission

Young magnetars are active. Their rapid rotation and strong magnetic field power wind outflows, and blast waves can also be launched from them into the wind outflows. When the blast waves interact with the outflowing materials, shocks will be formed. The shocks accelerate particles, leading to the radio emission as seen in the bursts from these systems. Such “shocks in magnetar outflows” is the scenario by Beloborodov (2017, 2020) has put forward in explaining the origin of FRBs. For FRB 20121102A, the magnetic field is required to be  $\geq 10^{14}$  Gauss (Cheng et al. 2020). With periodicities between a dozen and more than 100 days found in repeating FRBs, there is now a consensus that the burst periodicity is associated with either the orbital periods of binary systems, with the companion being a degenerate star or massive star, or the precession of a magnetar (Levin et al. 2020; Du et al. 2021; Rajwade & van den Eijnden 2023). And the possible origin of an ultra-long-period neutron star cannot be ruled out for FRBs with shorter periods (Beniamini et al. 2020; Kramer et al. 2023; Beniamini et al. 2023).

For FRB 20121102A, a highly eccentric binary orbit with a critical separation  $r_c \sim 7 \times 10^{13}$  cm (or 4.67 au) between the binary degenerates is assumed to account for its period of  $\sim 160$  days and a 50% burst duty cycle (Du et al. 2021). We adopt this geometric picture, in which the magnetized plasma

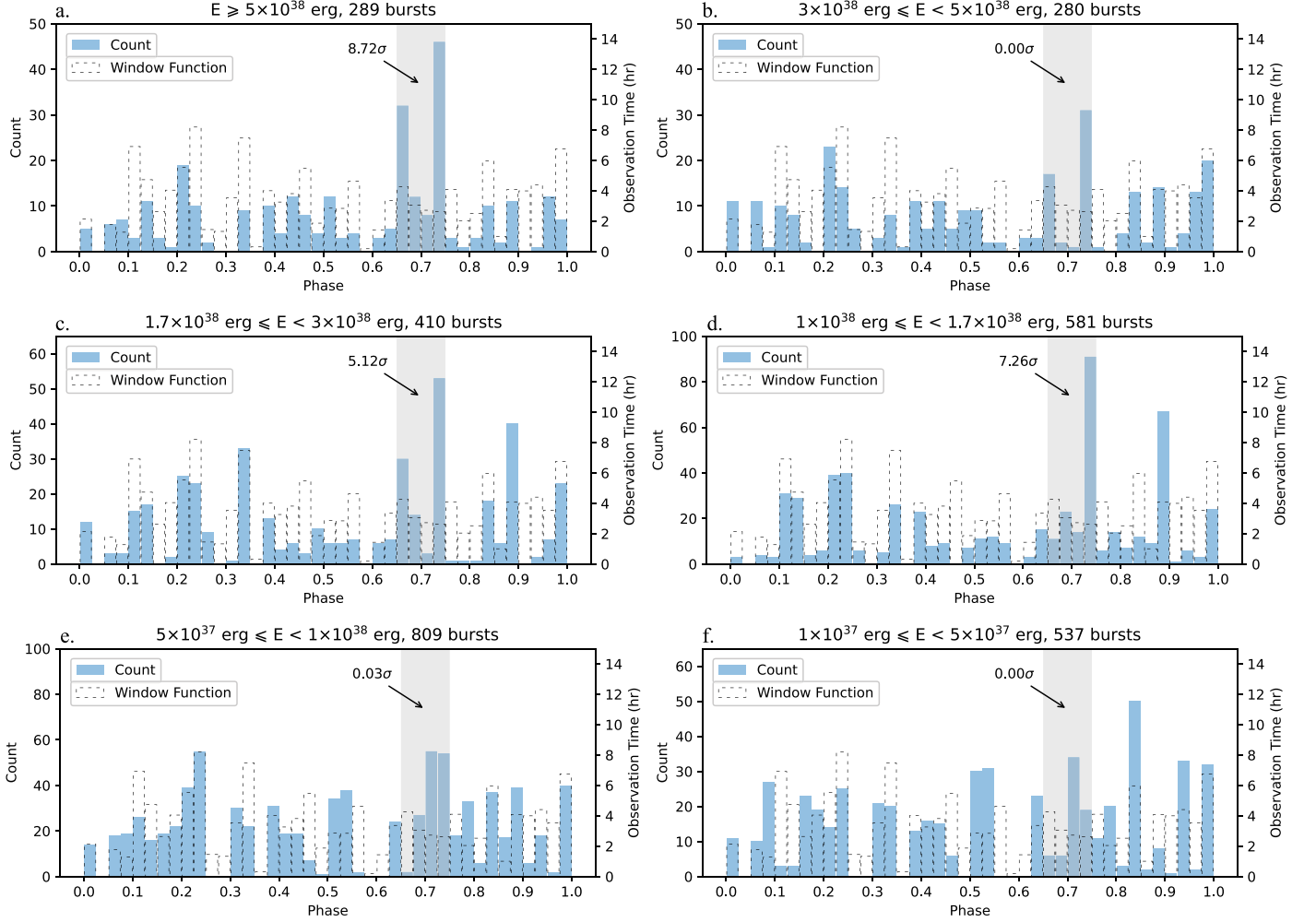


**Figure 5.** Phase distribution for the 4.605 day period for bursts observed with FAST and AO with different fluences. The blue and dashed black histograms show the burst counts and observation windows, respectively. The active phase is shown by the gray region, with the confidence level of the 4.605 day period indicated.

results from the accretion flow from the companion white dwarf and spreads between the companion and the neutron star when they have separations smaller than  $r_c$ . One possible explanation of the 4.605 day period is the existence of a planet close to the neutron star. For a neutron star of  $1.4 M_\odot$ , this period therefore implies a planet orbital separation of 0.061 au. Also, the planet will reside in the neutron star's magnetosphere and interact with the wind from the neutron star and the inflow material when the neutron star accretes. As such, the interaction between the planet and the magnetized plasma around it would form Alfvén wing instability, which gives rise to radio pulses, contributing to the quasiperiodic variations of single pulses observed in the FRB (Mottez & Zarka 2014; Mottez et al. 2020). Relativistic beaming makes the high-intensity radio bursts focus at a narrow range of direction. When the radiation direction passes through the line of sight in each planet orbit, increasing numbers of radio bursts are expected to be seen by the observer. Recalling the binary degenerate star system with the critical separation  $r_c$ , only when the binary interaction is on can there be accretion flows around the neutron star that hosts the planet, such that the planet is able to interact with the plasma around it to produce burst-like radio emission. In this scenario, using a model with two binary degenerate stars, where the neutron star has a closely orbiting planet, we are able to explain the  $\sim 160$  day period with a 50% duty cycle and the

4.605 day period for some of the high-energy bursts in a consistent manner.

Apart from the above scenario, there are other possible mechanisms for the bursts under the same geometric setting shown in Figure 9. We discuss them as supplementary models. The first alternative is magnetic reconnection. Magnetic field reconnections, like those observed in the solar system space environment (see, e.g., Hesse & Cassak 2020 for a review), convert the energy stored in magnetic fields to the kinetic energy of particles. Such high-energy particles can form Alfvén wings to produce coherent emission or radiate their energy away through processes such as curvature emissions by bunches (Zhang 2020a; Lyutikov 2021; Mahlmann et al. 2022; Wang et al. 2022). The condition of  $r < r_c$  for the binary degenerate star provides an environment of accretion flow or magnetar wind, in which there are enough charged particles for loading in the reconnection, giving rise to detectable radio bursts. Magnetic reconnection also occurs between the magnetar and the close-by planet if the planet is magnetized. Such reconnection can be modulated by the orbit of the planet, i.e., maximized when the strong magnetic field in the asymmetric planet magnetosphere faces the spinning magnetar (see Gao et al. 2020), leading to the 4.605 day quasi-period. The second alternative is unipolar induction. The tidal interaction between a rocky planet and its host star could



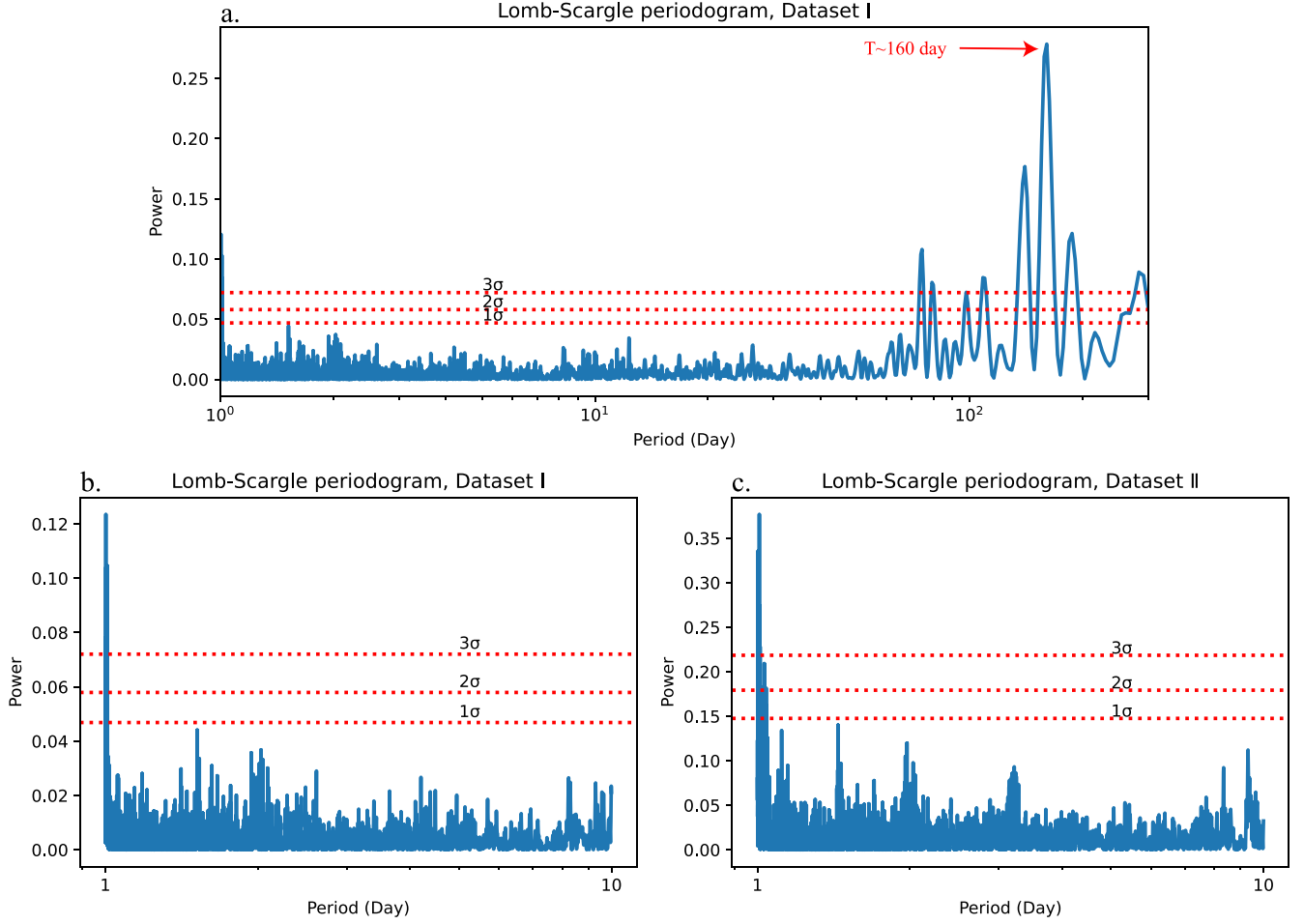


**Figure 6.** LS periodogram of data set I with test periods from 1 to 300 days (a) and of data set I (b) and data set II (c) with test periods from 1 to 10 days. The periodogram of data set I (a) shows a peak near the period  $T = 160$  days, in agreement with the results of Rajwade et al. (2020) and Cruces et al. (2018). In both (b) and (c), we can find the 1 day period arising from the observation window, but no peak around the period  $T = 4.6$  days is found.

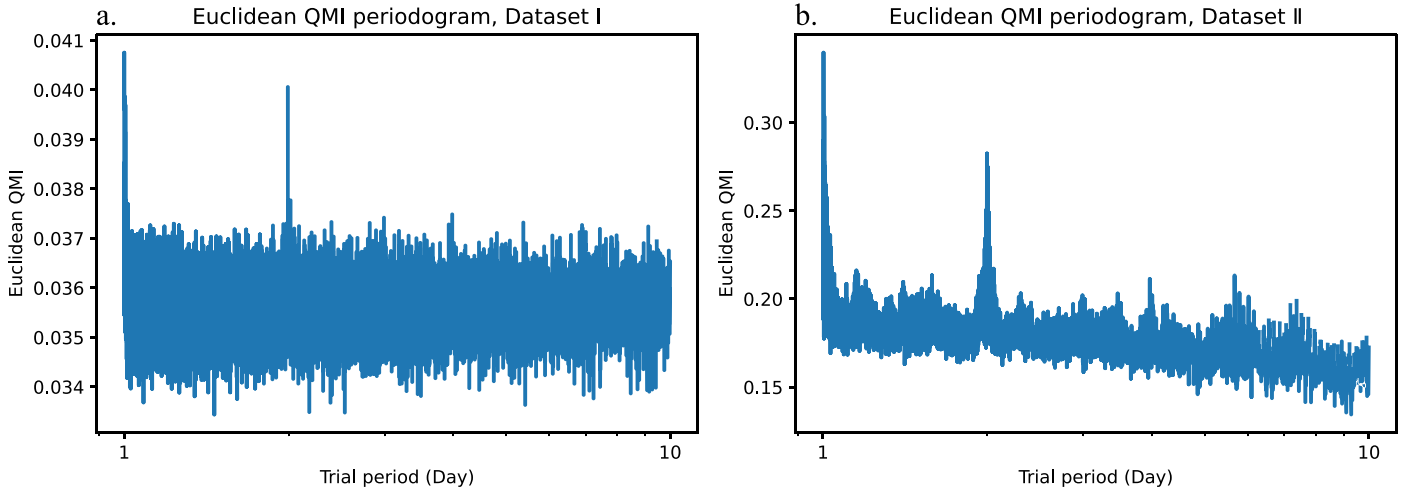


**Figure 7.** Euclidean QMI estimators of data set I (a) and data set II (b), with test periods from 1 to 10 days. We can see 1 and 2 day periods of the observation window in both panels, but no peak around the period  $T = 4.6$  days can be found.

cause volcanic activities, which will form unipolar induction and provide plasma around the planet for radio maser emission (Willes & Wu 2005; Laine & Lin 2012). However, the external plasma from accretion flows or magnetar wind in the binary

degenerate system usually contains high-energy particles, which are still crucial for the detectable high-fluence radio bursts. Thus, regardless of the scenarios proposed above, magnetic reconnection or even unipolar induction, the

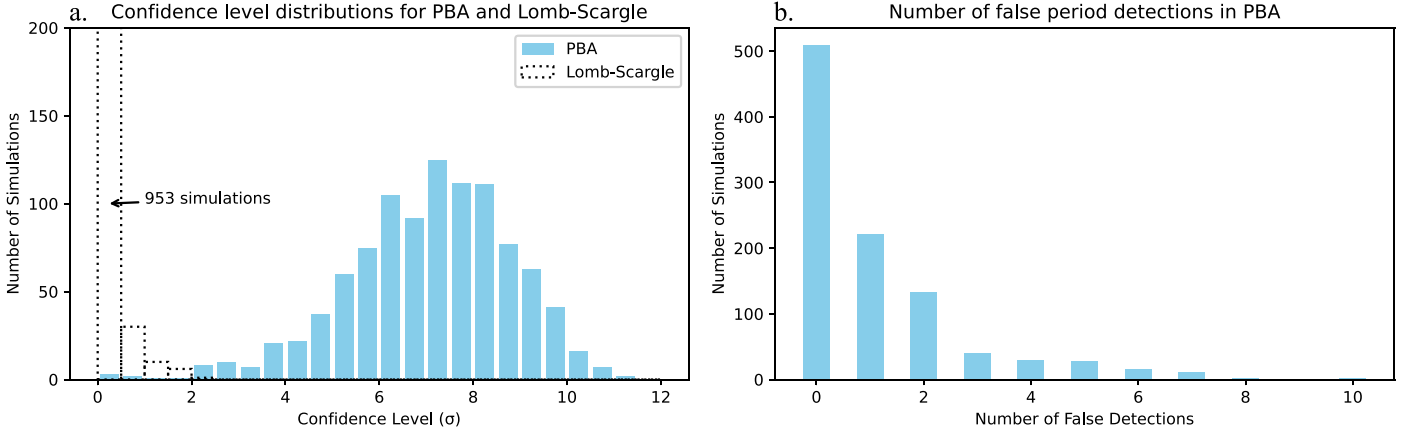


**Figure 8.** Results of PBA and the LS periodogram on burst data generated by Monte Carlo simulation. 1000 sets of burst data are generated by assuming 28% of bursts have a 0.1 duty cycle, a 4.605 day periodicity, and 72% are random and have no periodicity. In (a), the blue and dotted black histograms are the confidence levels for the 4.605 day period in PBA and LS, respectively. (b) shows the number of false period detections in PBA, with confidence levels higher than that of the 4.605 day period. The PBA method is more sensitive in detecting the 4.605 day period, without much confusion from false periods.

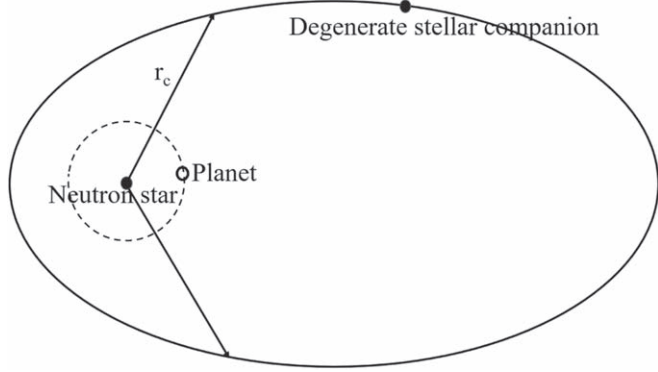


**Figure 9.** Schematic of possible origin of FRB 20121102A: a binary degenerate star system with a close-by planet around the primary neutron star. The binary has a highly eccentric orbit, with  $r_c$  the critical separation between the primary neutron star and the degenerate stellar companion, under which there are stellar wind or accretion interactions with the binary (Du et al. 2021). The close-by planet around the primary neutron star has an orbit period of  $\sim 4.6$  days. When there is accretion flow, it fills the space between the neutron star and the planet. In each planet orbit, when the radiation induced by the planet passes through the line of sight, high-intensity radio bursts focusing on a narrow range of direction are detected (Mottez et al. 2020).

geometrical configuration involving the binary degenerate with a neutron star hosting a closely orbiting planet (Figure 9) would be able to accommodate the periodicity of the bursts.

Consequently, the bursts from FRB 20121102A may be divided into two classes, arising from different processes. Most of the bursts, in particular, most low-energy bursts, and some high-energy bursts, arise from the shocks induced by magnetar blast waves interacting with the surrounding plasma. Simultaneously, a substantial fraction of high-energy bursts are caused by shock or the magnetic interaction between the magnetar and the planet closely orbiting around it, which produces more energetic particles compared to the shock in the surrounding plasma (Drain & McKee 1993), leading to more luminous radio bursts. This may explain the bimodal energy distribution in Li et al. (2021), consisting of a log-normal function for low-energy bursts and a generalized Lorentz–Cauchy function for high-energy ones. Despite the above speculative discussions, more burst properties, such as the dispersion measure and

rotation measure, should be further studied to reveal the origins of these two groups of bursts.

#### 4.2. Possible Formation of FRB 20121102A System

Another question is whether or not a system of such a configuration can be formed. It is almost certain that such a system cannot be formed by an encounter between two degenerate stars, with one carrying a planet. The encounter would immediately eject the planet, leaving a binary containing merely two degenerate stars. While there are studies that have shown that a free-floating planet can be captured by a star (Gouliniski & Ribakm 2018), it is possible that a binary containing two neutron stars or one neutron star and one white dwarf acting as a binary would give a larger capturing cross section than a single star (Wang et al. 2020). However, such a capture would result in a hierarchical system, with the planet in an outer orbit around two tightly bound degenerate stars. This kind of system would not give periodicities reconciling with what we have obtained for FRB 20121102A, which requires a hierarchy where the neutron star and the planet form a tight pair, with another degenerate star in the outer orbit. However, to produce such a hierarchy, it would be possible if a binary collided with a star carrying a planet. As described in Li et al. (2020), a binary of such a hierarchy could be produced by two possible channels. For the system of interest in this work, the initial and final configurations would be either

1.  $(\text{NS} + \text{p}) \otimes (\text{WD} + \text{X}) \rightarrow ((\text{NS} + \text{p}) + \text{WD}) \otimes \text{X}$ ; or
2.  $(\text{X} + \text{p}) \otimes (\text{WD} + \text{NS}) \rightarrow ((\text{NS} + \text{p}) + \text{WD}) \otimes \text{X}$ ,

where NS, WD, p, and X represent the neutron star, white dwarf, planet, and any kind of stellar object, respectively. The outcome in these two channels is that the star X would be ejected. Their main difference is that the second channel would go through an intermediate state, which determines whether the system will end up with an  $((\text{NS} + \text{p}) + \text{WD})$  hierarchy or an  $((\text{NS} + \text{WD}) + \text{p})$  hierarchy or something else. Stellar encounters are not rare in dense stellar environments, and multiple binary encounters are also expected to occur. Accessing the relative yields of the channels requires high-precision numerical calculations for the multiple stellar interactions covering a large parameter space. Depending on the formation chance, such a system may not be frequently seen in other FRB

repeaters. Instead, the binary degenerates or neutron star–planet system have a higher chance of presenting and may account for the repeating bursts of some FRBs.




## 5. Conclusions

Utilizing the PBA method, we have analyzed the quasiperiodicity of radio bursts from FRB 20121102A, compiled from the literature. We have identified a period of  $157.1^{+5.2}_{-4.8}$  days and a candidate period of  $4.605^{+0.003}_{-0.010}$  days, respectively. The former is consistent with previous findings and can be explained by the presence of a degenerate binary star system. The latter, also the focus of this work, is confirmed by two sets of data. It is more clearly seen in energetic bursts with fluences larger than  $1 \times 10^{38}$  erg. We attribute this to the possible presence of a planet closely orbiting one of the degenerate stars, presumably a neutron star. This dual origin of the bursts is supported by the bimodal distribution of the burst energy observed in FRB 20121102A. Shock waves and Alfvén wing instabilities induced by magnetic reconnection or unipolar induction near the planet are viable mechanisms for producing the radio emissions.

## Acknowledgments

We acknowledge the referee for professional discussions that helped us to improve the manuscript. This work was supported by the National Natural Science Foundation of China (NSFC# 11988101, 42150105, and 11725313); the National SKA Program of China (grant No. 2022SKA0120101); the Fundamental Research Funds for the Central Universities (Sun Yat-sen University, 2021qntd28, 22qntd3101); and the China Manned Space Project (No. CMS-CSST-2021-B09 and No. CMS-CSST-2021-B12). Y.G. acknowledges the support from the CSST Science Center for the Guangdong–Hongkong–Macau Greater Bay Area, SYSU, and the CAS Key Laboratory of FAST; K.W. acknowledges the support in part from the UK STFC through a Consolidate Grant awarded to UCL MSSL. This work has made use of the NASA ADS.

## ORCID iDs

Yang Gao  <https://orcid.org/0000-0002-6316-1632>  
Di Li  <https://orcid.org/0000-0003-3010-7661>  
Kinwah Wu  <https://orcid.org/0000-0002-7568-8765>

## References

- Beloborodov, A. M. 2017, *ApJL*, **843**, L26  
Beloborodov, A. M. 2020, *ApJ*, **896**, 142  
Beniamini, P., Wadiasingh, Z., Hare, J., et al. 2023, *MNRAS*, **520**, 1872  
Beniamini, P., Wadiasingh, Z., & Metzger, B. D. 2020, *MNRAS*, **496**, 3390  
Caleb, M., Stappers, B. W., Abbott, T. D., et al. 2020, *MNRAS*, **496**, 4565  
Carpano, S., Pollock, A. M. T., Prestwich, A., et al. 2007, *A&A*, **466**, L17  
Chatterjee, S., Law, C. J., Wharton, R. S., et al. 2017, *Natur*, **541**, 58  
Cheng, Y., Zhang, G. Q., & Wang, F. Y. 2020, *MNRAS*, **491**, 1498  
CHIME/FRB Collaboration, Andersen, B. C., Bandura, K., et al. 2023, *ApJ*, **947**, 83  
Cruces, M., Spitler, L. G., Scholz, P., et al. 2018, *MNRAS*, **500**, 448  
De Jager, O. C., & Büsching, I. 2010, *A&A*, **517**, L9  
De Jager, O. C., Swanepoel, J. W. H., & Raubenheimer, B. C. 1989, *A&A*, **221**, 180  
Drain, B. T., & McKee, C. F. 1993, *ARA&A*, **31**, 373  
Du, S., Wang, W., Wu, X., & Xu, R. 2021, *MNRAS*, **500**, 4678  
Dulk, G. A. 1985, *ARA&A*, **23**, 169  
Dworetzky, M. M. 1983, *MNRAS*, **203**, 917  
Forbes, C., Evans, M., Hastings, N., & Peacock, B. 2011, *Statistical Distributions* (4th ed.; Hoboken, NJ: Wiley)  
Gajjar, V., Siemion, A. P. V., Price, D. C., et al. 2018, *ApJ*, **863**, 2  
Gao, Y. 2021, *AJ*, **161**, 259  
Gao, Y., Qian, L., & Li, D. 2020, *ApJ*, **895**, 22  
Goulsinski, N., & Ribakm, E. N. 2018, *MNRAS*, **473**, 1589  
Gourdji, K., Michilli, D., Spitler, L. G., et al. 2019, *ApJL*, **877**, L19  
Hardy, L. K., Dhillon, V. S., Spitler, L. G., et al. 2017, *MNRAS*, **472**, 2800  
Hesse, M., & Cassak, P. M. 2020, *JGRA*, **125**, e25935  
Hessels, J. W. T., Spitler, L. G., Seymour, A. D., et al. 2019, *ApJL*, **876**, L23  
Hewitt, D. M., Snelders, M. P., Hessels, J. W. T., et al. 2022, *MNRAS*, **515**, 3577  
Hilmarsson, G. H., Michilli, D., Spitler, L. G., et al. 2021, *ApJL*, **908**, L10  
Horne, J. H., & Baliunas, S. L. 1986, *ApJ*, **302**, 757  
Huijse, P., Estévez, P. A., Förster, F., et al. 2018, *ApJS*, **236**, 12  
Jahns, J. N., Spitler, L. G., Nimmo, K., et al. 2023, *MNRAS*, **519**, 666  
Joseph, A., Chawla, P., Fonseca, E., et al. 2019, *ApJL*, **882**, L18  
Koen, C. 2006, *MNRAS*, **371**, 1390  
Kramer, M., Liu, K., Desvignes, G., Karuppusamy, R., & Stappers, B. W. 2023, *NatAs*, **8**, 230  
Kumar, P., Lu, W., & Bhattacharya, M. 2017, *MNRAS*, **468**, 2726  
Laine, R. O., & Lin, D. N. 2012, *ApJ*, **745**, 2  
Law, C. J., Abruzzo, M. W., Bassa, C. G., et al. 2017, *ApJ*, **850**, 76  
Leahy, D. A., Darbro, W., Elsner, F., et al. 1983, *ApJ*, **266**, 160  
Levin, Y., Beloborodov, A. M., & Bransgrove, A. 2020, *ApJL*, **895**, L30  
Li, D., Mustill, A. J., & Davies, M. N. 2020, *MNRAS*, **499**, 1212  
Li, D., Wang, P., Zhu, W. W., et al. 2021, *Natur*, **598**, 267  
Lorimer, D. R., Bailes, M., McLaughlin, M. A., Narkevic, D. J., & Crawford, F. A. 2007, *Sci*, **318**, 777  
Lu, W., Kumar, P., & Zhang, B. 2020, *MNRAS*, **498**, 1397  
Lyutikov, M. 2021, *ApJ*, **922**, 166  
Lyutikov, M., Barkov, M. V., & Giannios, D. 2020, *ApJL*, **893**, L39  
Mahlmann, J. F., Philippov, A. A., Levinson, A., Spitkovsky, A., & Hakobyan, H. 2022, *ApJL*, **932**, L20  
Majid, W. A., Pearlman, A. B., Nimmo, K., et al. 2020, *ApJL*, **897**, L4  
Marcote, B., Paragi, Z., Hessels, J. W. T., et al. 2017, *ApJL*, **834**, L8  
Metzger, B. D., Margalit, B., & Sironi, L. 2019, *MNRAS*, **485**, 4091  
Michilli, D., Seymour, A., Hessels, J. W. T., et al. 2018, *Natur*, **553**, 182  
Mottez, F., & Zarka, P. 2014, *A&A*, **569**, A86  
Mottez, F., Zarka, P., & Voisin, G. 2020, *A&A*, **644**, A145  
Niu, C.-H., Aggarwal, K., Li, D., et al. 2022, *Natur*, **606**, 873  
Oostrum, L. C., Maan, Y., van Leeuwen, J., et al. 2020, *A&A*, **635**, A61  
Pearlman, A. B., Majid, W. A., Prince, T. A., et al. 2020, *ApJL*, **905**, L27  
Pérez-Torres, M., Gómez, J. F., Ortiz, J. L., et al. 2021, *A&A*, **645**, A77  
Petroff, E., Hessels, J. W. T., & Lorimer, D. R. 2022, *A&ARv*, **30**, 2  
Pleunis, Z., Michilli, D., Bassa, C. G., et al. 2021, *ApJL*, **911**, L3  
Rajwade, K. M., Mickaliger, M. B., Stappers, B. W., et al. 2020, *MNRAS*, **495**, 3551  
Rajwade, K. M., & van den Eijnden, J. 2023, *A&A*, **673**, 136  
Scholz, P., Bogdanov, S., Hessels, J. W. T., et al. 2017, *ApJ*, **846**, 80  
Scholz, P., Spitler, L. G., Hessels, J. W. T., et al. 2016, *ApJ*, **833**, 177  
Spitler, L. G., Herrmann, W., Bower, G. C., et al. 2018, *ApJ*, **863**, 150  
Spitler, L. G., Scholz, P., Hessels, J. W. T., et al. 2016, *Natur*, **531**, 202  
The CHIME/FRB Collaboration 2020, *Natur*, **582**, 351  
VanderPlas, J. T. 2018, *ApJS*, **236**, 16  
Wang, W.-Y., Yang, Y.-P., Niu, C.-H., Xu, R., & Zhang, B. 2022, *ApJ*, **927**, 105  
Wang, Y.-H., Perna, R., & Leigh, N. W. C. 2020, *MNRAS*, **496**, 1453  
Willes, A. J., & Wu, K. 2005, *A&A*, **432**, 1091  
Zarka, P., Marques, M. S., Louis, C., et al. 2018, *A&A*, **618**, A84  
Zhang, B. 2020a, *ApJL*, **890**, L24  
Zhang, B. 2020b, *Natur*, **582**, 344  
Zhang, B. 2020c, *Natur*, **587**, 45  
Zhang, Y. G., Gajjar, V., Foster, G., et al. 2013, *ApJ*, **866**, 149  
Zhang, Y.-K., Li, D., Feng, Y., et al. 2024, *SciBu*, **69**, 1020